

# Spin-Transfer Pathways in Paramagnetic Lithium Transition-Metal Phosphates from Combined Broadband Isotropic Solid-State MAS NMR Spectroscopy and DFT Calculations

Raphaële J. Clément,<sup>†,‡</sup> Andrew J. Pell,<sup>†</sup> Derek S. Middlemiss,<sup>‡</sup> Fiona C. Strobridge,<sup>‡</sup> Joel K. Miller,<sup>§</sup> M. Stanley Whittingham,<sup>§</sup> Lyndon Emsley,<sup>†</sup> Clare P. Grey,<sup>‡</sup> and Guido Pintacuda<sup>\*,†</sup>

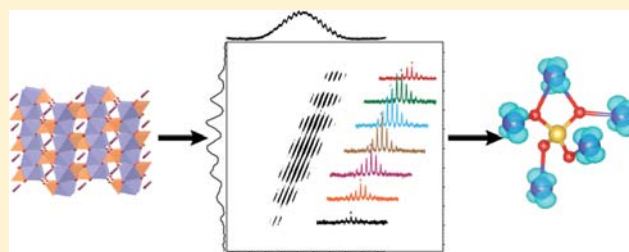
<sup>†</sup>Centre de RMN à Très Hauts Champs, UMR 5280 CNRS/Ecole Normale Supérieure de Lyon/UCB, Lyon 1, 69100 Villeurbanne, France

<sup>‡</sup>Department of Chemistry, University of Cambridge, Lensfield Road, Cambridge, CB2 1EW, United Kingdom

<sup>§</sup>Department of Chemistry, State University of New York at Binghamton, Binghamton, New York 13902-6000, United States

## Supporting Information

**ABSTRACT:** Substituted lithium transition-metal (TM) phosphate  $\text{LiFe}_x\text{Mn}_{1-x}\text{PO}_4$  materials with olivine-type structures are among the most promising next generation lithium ion battery cathodes. However, a complete atomic-level description of the structure of such phases is not yet available. Here, a combined experimental and theoretical approach to the detailed assignment of the  $^{31}\text{P}$  NMR spectra of the  $\text{LiFe}_x\text{Mn}_{1-x}\text{PO}_4$  ( $x = 0, 0.25, 0.5, 0.75, 1$ ) pure and mixed TM phosphates is developed and applied. Key to the present work is the development of a new NMR experiment enabling the characterization of complex paramagnetic materials via the complete separation of the individual isotropic chemical shifts, along with solid-state hybrid DFT calculations providing the separate hyperfine contributions of all distinct Mn–O–P and Fe–O–P bond pathways. The NMR experiment, referred to as aMAT, makes use of short high-powered adiabatic pulses (SHAPs), which can achieve 100% inversion over a range of isotropic shifts on the order of 1 MHz and with anisotropies greater than 100 kHz. In addition to complete spectral assignments of the mixed phases, the present study provides a detailed insight into the differences in electronic structure driving the variations in hyperfine parameters across the range of materials. A simple model delimiting the effects of distortions due to Mn/Fe substitution is also proposed and applied. The combined approach has clear future applications to TM-bearing battery cathode phases in particular and for the understanding of complex paramagnetic phases in general.



## 1. INTRODUCTION

The increasingly widespread use of battery-powered plug-in electric and all-electric vehicles and the development of batteries for storage on the electric grid require new, cheaper, and safer electrode materials with higher energy densities. One class of compounds that is currently of particular interest for lithium ion batteries is composed of the olivine-type materials  $\text{LiFe}_x\text{Mn}_{1-x}\text{PO}_4$ <sup>1</sup> (LFMP, Figure 1a), which are formed by the mixing of the pure  $\text{LiMnPO}_4$  (LMP) and  $\text{LiFePO}_4$  (LFP) phases. There is an increasing realization that the pure Fe material does not have a sufficiently high energy density for many applications (the  $\text{Fe}^{2+/3+}$  redox couple lying at 3.4 V vs  $\text{Li}^+/\text{Li}$ ), and so much work has been expended to activate the higher voltage materials ( $M = \text{Mn}$  and  $\text{Co}$ ,  $M^{2+/3+}$  lying at 4.1 and 4.8 V, respectively, vs  $\text{Li}^+/\text{Li}$ ).<sup>2</sup> Solid solutions of Fe with other transition metals (TMs) generally show better electrochemical performance than the Mn- and Co-only materials, a phenomenon that is generally attributed to the local and long-range distortions caused by cation substitution. Local structural distortions are thus key to understanding the electrochemical properties of these materials.

Most studies of these materials have used long-range structural methods, such as X-ray diffraction (XRD), while local probes of structure have largely focused on the environments around the TM ions. Previous XRD studies typically concur that the various LFMP stoichiometries are all solid solutions of LFP and LMP,<sup>3–7</sup> albeit with impurity phase profiles and Li–TM antisite defect concentrations showing some dependence on Fe/Mn ratio. X-ray absorption near-edge spectroscopy and extended X-ray absorption fine structure (XANES and EXAFS, respectively) studies have also been undertaken, focusing mainly upon the evolution of local structure and phase transformations occurring with electrochemical cycling.<sup>8,9</sup> Recently there has also been interest in the electrochemical properties of specific morphologies of LFMP, such as nanorods<sup>10</sup> and nanoplates.<sup>11</sup>

In principle solid-state nuclear magnetic resonance (NMR) spectroscopy using  $^{31}\text{P}$  and  $^6,7\text{Li}$  is ideal for the investigation of the local distortions and variations in electronic structures

Received: July 14, 2012

Published: September 24, 2012

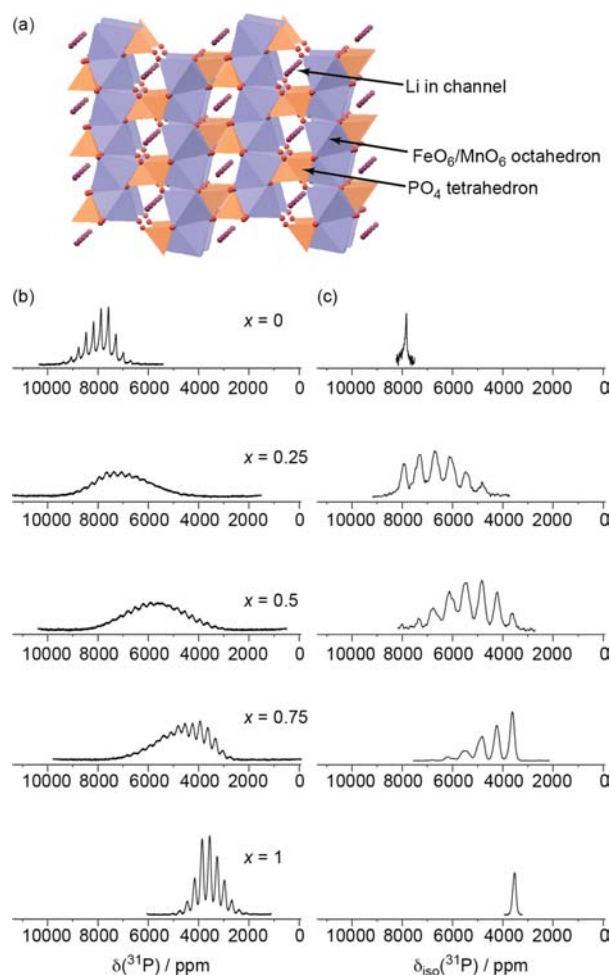


**Figure 1.**  $^{31}\text{P}$  NMR spectra of the five  $\text{LiFe}_x\text{Mn}_{1-x}\text{PO}_4$  compounds ( $x = 0, 0.25, 0.5, 0.75, 1$ ), all of which occur in the olivine-type structure which is shown in (a). The one-dimensional spectra containing overlapping sideband patterns are shown in (b), and the projections of the aMAT spectrum containing just the isotropic shifts are shown in (c).

associated with both TM substitution and delithiation.<sup>12</sup> Indeed, solid-state NMR spectroscopy is a well-established method for the characterization of the structures of a wide variety of systems in modern chemistry, biology, and material sciences.<sup>13–16</sup> However, acquiring  $^{31}\text{P}$  NMR spectra from these materials is challenging for the reason that the paramagnetic TM ions induce both very large paramagnetic shifts and shift anisotropies of the order of 100–10 000 ppm,<sup>17,18</sup> along with substantial inhomogeneous broadening due to temperature gradients and anisotropic bulk magnetic susceptibility (ABMS) effects,<sup>19</sup> resulting in very broad spectra.<sup>20</sup> While such interactions are not intrinsically deleterious, and may on the contrary provide a wealth of structural information, their presence often makes it very difficult to acquire spectra since the broadening of the resonances makes broadband excitation impossible with conventional radio frequency (RF) pulses at practicable field amplitudes. The broadening also leads to very low sensitivity. The result is that spectra are often essentially unobservable. The shift interactions scale with the strength of the external field, and so one practical approach is to acquire spectra using low-field spectrometers (e.g., corresponding to a  $^1\text{H}$  Larmor frequency of 100–300 MHz). However low-field NMR experiments exacerbate the sensitivity issues.

It has been shown that there can be a spectacular improvement in the sensitivity and resolution of NMR spectra under high-field conditions by applying ultrafast magic-angle spinning (MAS) and short recycle delays.<sup>21–23</sup> Furthermore, the excitation problem has been addressed through recent progress in the development and application of adiabatic-pulse schemes for spinning solids, allowing broadband excitation limited only by the bandwidth of the probe.<sup>24–28</sup> A further advantage of adiabatic pulses is that, provided the RF field is sufficiently high to deliver adiabatic<sup>29</sup> or superadiabatic<sup>30</sup> inversion, the pulses have a high tolerance to RF field inhomogeneity. In particular there are two specific schemes that have been found to deliver impressive results, namely short high-powered adiabatic pulses (SHAPs),<sup>24</sup> and single-sideband-selective adiabatic pulses (S<sup>3</sup>APs).<sup>25–28</sup> In the best cases these schemes can deliver complete inversion over a range of frequencies that is at least an order of magnitude greater than the RF field.

A remaining barrier to the interpretation of the NMR spectra is that the spinning sideband patterns of the different sites can often overlap very extensively, a problem that is particularly severe at higher fields where the number of sidebands increases. There are a number of experiments designed to separate overlapping sideband patterns, of which the most widely used are the phase alternating sideband separation (PASS)<sup>31–33</sup> and magic-angle turning (MAT)<sup>34,35</sup> sequences. However both of these sequences employ a train of five  $180^\circ$  pulses and do not achieve the uniform broadband inversion necessary to obtain a quantitative spectrum in paramagnetic materials. It has recently been shown that a larger excitation bandwidth can be obtained with the MATPASS sideband separation experiment which uses a train of conventional pulses with a  $90^\circ$  flip angle.<sup>36</sup> The  $90^\circ$  experiment however suffers from low sensitivity, due to the retention of only a fraction of the signal components, and the accumulation of the effects of RF inhomogeneity from the use of a train of such pulses.

Here we describe a combined experimental and theoretical approach to the acquisition and interpretation of the  $^{31}\text{P}$  NMR spectra of the technologically relevant  $\text{LiFe}_x\text{Mn}_{1-x}\text{PO}_4$  ( $x = 0, 0.25, 0.5, 0.75, 1$ ) cathode phases. First, a new NMR experiment is developed and applied that offers the possibility of completely removing the overlap between the sideband manifolds for paramagnetic samples over broad bandwidths. This experiment incorporates the SHAPs into the MAT pulse sequence, and so we refer to it as the adiabatic MAT or aMAT experiment. It is shown here to give impressive results, efficiently separating isotropic shifts over a range of the order of 1 MHz with shift anisotropies of the order of hundreds of kHz. Second, solid-state hybrid density functional theory (DFT) calculations are applied to determine the hyperfine (Fermi contact) parameters of all distinct TM–O–P bond pathways in the pure LMP and LFP phases. Third, the aMAT spectra of the LFMP phases are successfully fitted by a random solution model starting from the DFT-derived hyperfine parameters of the pure LMP and LFP phases. A simple model delimiting the likely effects of the distortions induced by TM mixing is also proposed and applied. A full and convincing assignment of all spectral features is achieved for each phase, opening up the possibility of the further interpretation of the key redox processes and phase transformations occurring in such materials on electrochemical cycling.

## 2. EXPERIMENTAL SECTION

**2.1. Sample Preparation.** The  $\text{LiFe}_x\text{Mn}_{1-x}\text{PO}_4$  samples were prepared by hydrothermal synthesis by using  $\text{FeSO}_4 \cdot 7\text{H}_2\text{O}$ ,  $\text{MnSO}_4 \cdot \text{H}_2\text{O}$  (both 98% Fisher),  $\text{H}_3\text{PO}_4$  (85 wt % solution Fisher) and  $\text{LiOH}$  (98% Aldrich) in the stoichiometric ratios  $x:1.0-x:3.0:1.0$ , as described previously in the literature.<sup>37,38</sup>  $\text{MnSO}_4 \cdot \text{H}_2\text{O}/\text{FeSO}_4 \cdot \text{H}_2\text{O}$  and  $\text{H}_3\text{PO}_4$  were mixed first, and then 1.3 g/L of sugar and/or L-ascorbic acid (99% Aldrich) was added as an in situ reducing agent to minimize the oxidation of  $\text{Fe}^{2+}$ . Multiwall carbon nanotubes (95% Aldrich), 0.8 g/L, were also added. After  $\text{LiOH}$  addition, the resulting gel was heated at 180–200 °C for 5 h to 2 days, and the precipitates were collected by suction filtration and dried at 60 °C for 3 h under vacuum.

**2.2.  $^{31}\text{P}$  NMR.** All NMR spectra were acquired on a Bruker 500 Avance III spectrometer operating at a Larmor frequency of 202 MHz for  $^{31}\text{P}$ . The one-dimensional  $^{31}\text{P}$  spectra were recorded using a double-adiabatic spin–echo sequence employing a pair of tanh/tan SHAPs,<sup>24,39</sup> each sweeping through 5 MHz in 50  $\mu\text{s}$  with a RF amplitude of 417 kHz. For each spectrum, 32 768 scans were acquired using a recycle delay of 100 ms. All experiments were carried out at a sample temperature estimated to be 320 K.

The  $^{31}\text{P}$  aMAT spectra (sequence shown in Figures 2b and S2b) employed the same SHAPs as for the one-dimensional spectra. The

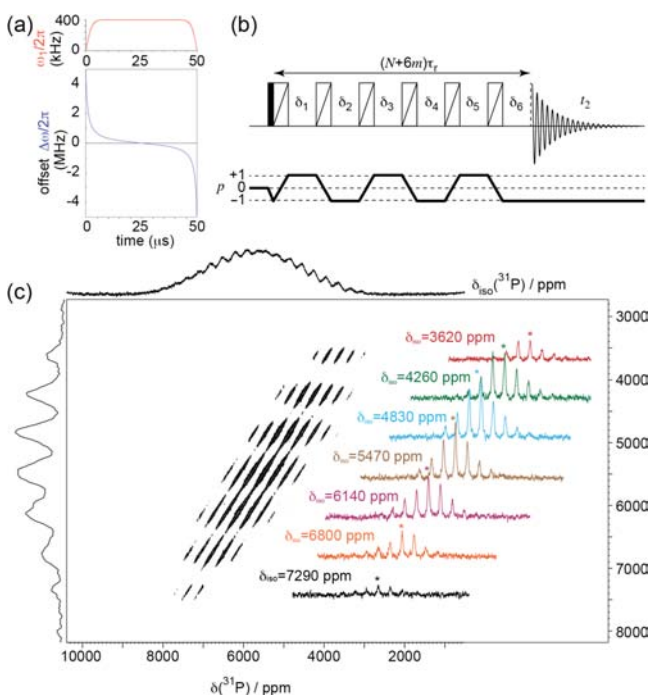


**Figure 2.** The two-dimensional aMAT experiment. The amplitude and transmitter offset profiles of the tanh/tan SHAP are given in (a).<sup>24,39</sup> Each SHAP has a duration of  $m$  rotor periods, where  $m = 3$  (50  $\mu\text{s}$ ) in this case. These are incorporated into the pulse sequence in (b). The solid rectangle is a conventional  $90^\circ$  pulse, and the open rectangles with diagonal strokes represent the SHAPs. The overlapping sideband patterns in the one-dimensional  $^{31}\text{P}$  spectrum of  $\text{LiFe}_{0.5}\text{Mn}_{0.5}\text{PO}_4$  ( $x = 0.5$ ) are separated in the two-dimensional spectrum in (c), in which the indirect dimension contains just the isotropic shifts. The seven resolved sideband patterns are also shown.

spectra of the three mixed-phase compounds were recorded with an aMAT recoupling time of 7 rotor periods (116.67  $\mu\text{s}$ ), excluding the lengths of the SHAPs. Using the echo/antiecho scheme,<sup>40,41</sup> 150 complex increments were acquired and processed. The spectral width in the indirect dimension is 1.25 MHz. The number of scans per increment for each spectrum was 5920 ( $x = 0.75$ ), 2656 ( $x = 0.5$ ), and 4512 ( $x = 0.25$ ).

The aMAT spectra of the two pure-phase compounds were recorded with an aMAT recoupling time of 13 rotor periods (216.67  $\mu\text{s}$ ), and 32 complex increments were acquired. The spectral width in the indirect dimension is 148 kHz. The number of scans per increment was 7552 for  $\text{LiFePO}_4$  and 9760 for  $\text{LiMnPO}_4$ .

**2.3. Fitting of the  $^{31}\text{P}$  Isotropic aMAT Projections.** The three spectra of the mixed samples were fitted by varying the differences between the contributions of  $\text{Mn}^{2+}$  and  $\text{Fe}^{2+}$  for each of the five TM–O–P pathways in the first TM coordination shell, as described in Section 3.2, and the total contact shift of the all- $\text{Fe}^{2+}$  environment. The line shape and width of all 32 peaks were taken from the peak at 3625 ppm, which the DFT calculations indicate is a single completely resolved site, as described below. The use of the same line shape for all sites is justified on the basis that the line broadening in the projection is entirely due to inhomogeneous contributions, which we expect to be dominated by bulk rather than local effects. The relative intensities of each of the 32 model peaks were calculated in two steps. First, the intensities are assumed proportional to the stoichiometry-dependent probabilities of the configurations calculated on the basis of a random distribution of  $\text{Fe}^{2+}$  and  $\text{Mn}^{2+}$ . Second, the intensities are further weighted to account for the differential dephasing of the coherences of different  $^{31}\text{P}$  sites during the aMAT recoupling period, using the experimental coherence lifetimes ( $T_2'$ ) of the pure  $\text{LiMnPO}_4$  and  $\text{LiFePO}_4$  compounds, as described more fully in the SI.

**2.4. DFT Calculations.** First-principles solid-state DFT calculations were performed within the CRYSTAL09 linear combinations of atomic orbitals code.<sup>42</sup> Two hybrid functionals were used: the B3LYP functional bearing 20% Hartree–Fock (HF) exchange (hyb20) with a previously demonstrated satisfactory performance for the electronic structure and band gaps of a broad range of materials,<sup>43</sup> and for the properties of transition-metal compounds in particular,<sup>44</sup> and a related 35% HF hybrid (hyb35) previously shown to provide magnetic coupling constants in good agreement with experimental values.<sup>45–47</sup>

In addition, recent calculations on various  $\text{Fe}^{3+}$  phosphates suggest that hybrid functionals bearing weights of HF exchange in the range from 20 to 35% provide hyperfine shifts in good agreement with experiment.<sup>20</sup> Electron–nuclear hyperfine parameters for  $^{31}\text{P}$  sites have been computed by a method identical to that adopted in our recent study of  $\text{Fe}^{3+}$  phosphates.<sup>20</sup> Briefly, the Fermi contact contribution to the hyperfine shift is computed from the spin density directly at the nuclear position in the ferromagnetic state and subsequently scaled to a value consistent with the paramagnetic state in which the experiments were performed by multiplication by a factor  $\Phi = B_0 \mu_{\text{eff}}^2 / 3k_B g_e \mu_B S(T - \Theta)$ , where  $B_0$  is the static magnetic induction,  $\mu_{\text{eff}}$  is the experimental effective magnetic moment per TM site,  $S$  is the formal spin of the metal species (equal to 5/2 for  $\text{Mn}^{2+}$  and 2 for  $\text{Fe}^{2+}$ ),  $k_B$  is the Boltzmann constant,  $g_e$  is the free electron  $g$ -value,  $\mu_B$  is the Bohr magneton,  $T$  is the experimental temperature (assumed equal to 320 K throughout to account for frictional heating due to MAS), and  $\Theta$  is the experimental Weiss constant. TM–O–P bond pathway decompositions of total hyperfine shifts are performed by the flipping of selected TM spins in  $\text{Li}_8\text{M}_8(\text{PO}_4)_8$  supercells, where the differences in  $^{31}\text{P}$  contact shifts due to the flip directly yield the symmetry distinct pathway contributions. Full details of the DFT calculations and hyperfine models including the basis sets, numerical parameters, and experimental  $\mu_{\text{eff}}$  and  $\Theta$  parameters<sup>48,49</sup> used are presented in the SI.

## 3. RESULTS AND DISCUSSION

### 3.1. $^{31}\text{P}$ MAT of LFMP with SHAPs (aMAT Sequence).

One-dimensional  $^{31}\text{P}$  double-adiabatic spin–echo spectra of the five  $\text{LiFe}_x\text{Mn}_{1-x}\text{PO}_4$  materials ( $x = 0, 0.25, 0.5, 0.75, 1$ ) were acquired at 60 kHz MAS as shown in Figure 1b. The isotropic shifts in the corresponding  $^{31}\text{P}$  spectra cover a frequency range that is an order of magnitude larger than the inhomogeneous broadening. The  $^{31}\text{P}$  spectrum of the  $x = 0$  compound exhibits a sideband pattern from a single site with an isotropic shift of 7879 ppm. The magnetic susceptibility tensor of the  $d^5 \text{Mn}^{2+}$

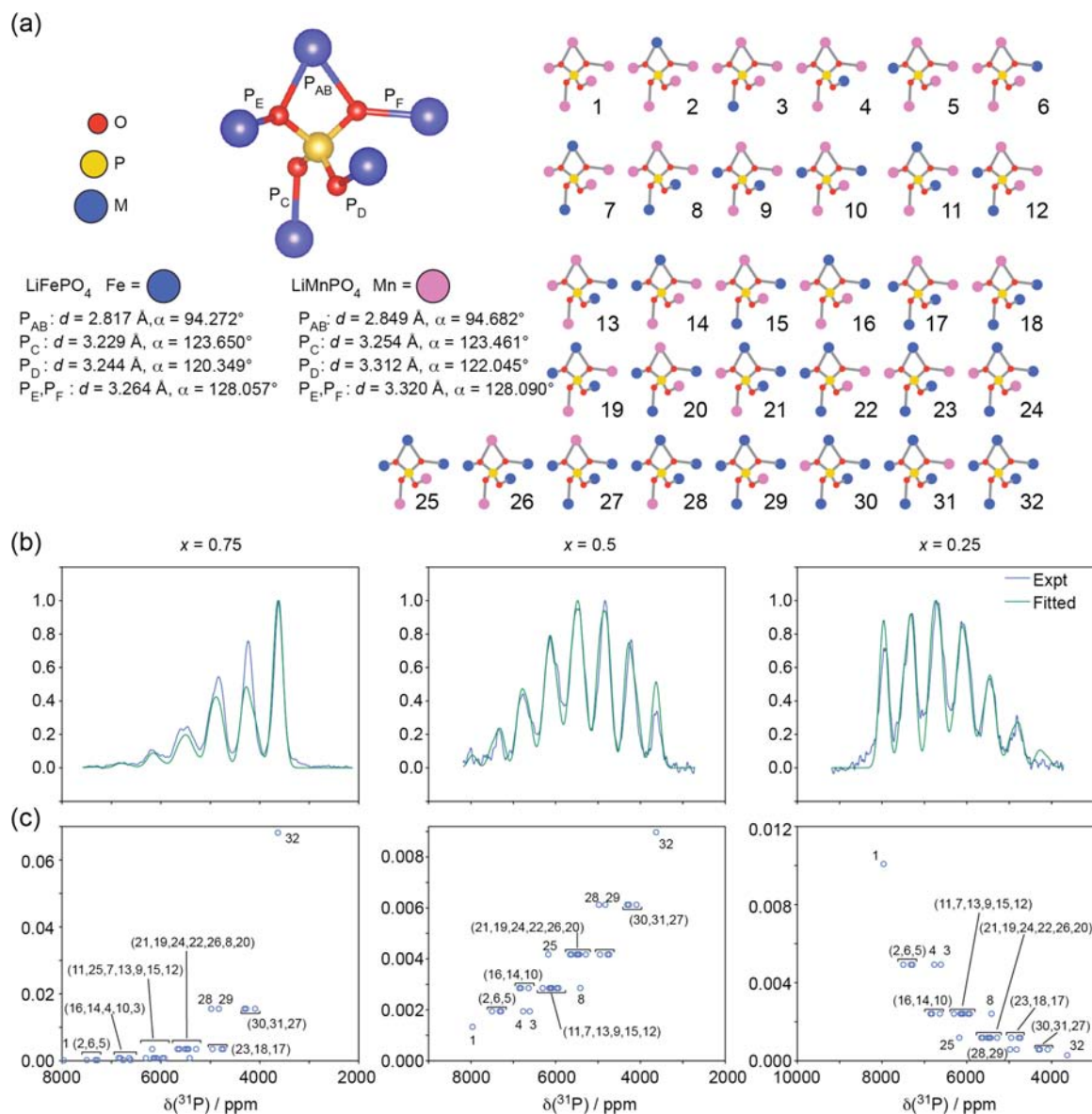


**Figure 3.** Results of the fitting described in the text. Pathway contributions of the  $\text{Mn}^{2+}$  and  $\text{Fe}^{2+}$  ions to the total contact shift were varied to fit the isotropic projections of the experimental  $^{31}\text{P}$  NMR spectra. TM–O–P pathway labels, distances ( $d$ ) and bond angles ( $\alpha$ ) in LMP and LFP are shown in (a) together with the 32 possible configurations in the mixed  $\text{Mn}^{2+}/\text{Fe}^{2+}$  phases. The comparison of the experimental and fitted isotropic spectra is shown in (b) for the  $x = 0.75$ ,  $0.5$ , and  $0.25$  phases. The contact shifts and relative intensities of the 32 peaks occurring in each spectrum are shown in the absence of line shape effects in (c), with labeling as in (a). The intensities shown in (c) take into account both the stoichiometry-dependent probability of the configuration and the relaxation effects.

ion is expected to be isotropic, and so the paramagnetic shift might reasonably be wholly attributed to the Fermi contact interaction. The corresponding sideband pattern in the spectrum of the  $x = 1$  compound has a lower isotropic shift of 3558 ppm. Here, however, the  $d^6$   $\text{Fe}^{2+}$  susceptibility tensor is anticipated to be anisotropic, and so this shift will likely contain contributions due to both the Fermi contact and pseudocontact mechanisms, of which the former is expected to dominate given the large  $^{31}\text{P}$  shifts typical in such phases. The wide variety of environments occurring in each of the three mixed phases leads to multiple resonances, which combine to produce a complex set of overlapping sideband patterns. As a result of the extensive overlap, it is nontrivial to obtain a site-specific assignment or useful interpretation of these data alone. Complete separation of the sideband manifolds is needed to retrieve the site-specific shifts.

The aMAT pulse sequence (shown in Figure 2b) is a modification of the standard five  $180^\circ$  pulse MAT experiment<sup>34,35</sup> in which the five conventional refocusing  $180^\circ$  pulses are replaced with tanh/tan SHAPs, the amplitude and offset profiles of which are shown in (a).<sup>24,39</sup> A sixth  $180^\circ$  SHAP pulse is added immediately after the conventional  $90^\circ$  excitation. This extra pulse is a key element that plays two roles. First, a property of adiabatic refocusing pulses is that they are properly effective only when used in pairs.<sup>50</sup> When used alone, they fail to refocus and lead to a large phase distortion. To adapt the five pulse MAT experiment to adiabatic refocusing pulses, we thus need to add the additional  $180^\circ$  pulse. Second, the adiabatic double echo would normally only refocus the anisotropic part of the interactions if the delay between the pulses is an integer multiple of the rotor period. This would be a severe limitation on bandwidth in the isotropic

**Table 1. Comparison of the Best-Fit and DFT Calculated (hyb20 and hyb35) Differences in Pathway Contributions  $\Delta\epsilon^P$  for Each of the Five TM–O–P Pathways in the First Coordination Shell of the P Sites and the Total Contact Shift of the Configurations in which  $\text{Fe}^{2+}$  and  $\text{Mn}^{2+}$  Occupy All Five Neighboring TM Sites<sup>a</sup>**

(ppm)	shifts of pure TM configurations in LFP and LMP		differences in pathway contributions				
	$\delta(\text{Fe})$	$\delta(\text{Mn})$	$\Delta\epsilon^{\text{AB}}$	$\Delta\epsilon^{\text{C}}$	$\Delta\epsilon^{\text{D}}$	$\Delta\epsilon^{\text{E}}$	$\Delta\epsilon^{\text{F}}$
hyb20	3629 <sup>b</sup> –4385 <sup>c</sup>	8660 <sup>d</sup> –10 551 <sup>e</sup>	441 <sup>c,d</sup> –587 <sup>b,e</sup>	1725 <sup>c,d</sup> –2077 <sup>b,e</sup>	1316 <sup>b,d</sup> –1665 <sup>c,e</sup>	320 <sup>c,d</sup> –1373 <sup>b,e</sup>	320 <sup>c,d</sup> –1373 <sup>b,e</sup>
hyb35	2899 <sup>b</sup> –3517 <sup>c</sup>	7236 <sup>d</sup> –8804 <sup>e</sup>	343 <sup>c,d</sup> –453 <sup>b,e</sup>	1537 <sup>c,d</sup> –1821 <sup>b,e</sup>	1142 <sup>b,d</sup> –1442 <sup>c,e</sup>	274 <sup>c,d</sup> –1169 <sup>b,e</sup>	274 <sup>c,d</sup> –1169 <sup>b,e</sup>
fitted	3631(3)	7931(41)	461(4)	1350(2)	1201(5)	644(29)	644(28)

<sup>a</sup>The ranges in total shifts and pathway contributions correspond to the extremal values obtained by the substitution of  $\text{Fe}^{2+}$  and  $\text{Mn}^{2+}$  into both fixed LMP and LFP structures, with combinations indicated by superscripts. The labeling of the five TM–O–P pathways is as shown in Figure 3a. The standard errors in the fitted parameters are shown in parentheses. <sup>b</sup> $\text{Fe}@LMP$ . <sup>c</sup> $\text{Fe}@LFP$ . <sup>d</sup> $\text{Mn}@LMP$ . <sup>e</sup> $\text{Mn}@LFP$ .

dimension. However, the symmetry of the six 180° pulse experiment is such that refocusing of the anisotropic component is achieved for any value of the pulse spacing, thus allowing large spectral widths in the indirect (isotropic) dimension (see the SI for a full explanation). The resulting aMAT experiment offers a tremendous improvement in the bandwidth compared to conventional pulse experiments at the same RF field (see Figure S6 for comparisons of the inversion profiles), with 100% inversion being obtained for bandwidths of a few MHz in the best cases.

As for the conventional MAT sequence, the indirect dimension of the two-dimensional spectrum contains only the isotropic resonances, with the sidebands being suppressed. The isotropic resonances are correlated with the conventional one-dimensional spectrum in the direct dimension. This is shown in the plot of the two-dimensional <sup>31</sup>P aMAT spectrum of the  $x = 0.5$  phase in Figure 2c, where the one-dimensional spectrum is now separated into a series of seven resolved isotropic peaks, each of which correlates with a resolved sideband pattern. A further feature of the two-dimensional spectrum is that the inhomogeneous contribution to the line broadening is correlated along the main diagonal. Since this broadening dominates the line shape of the individual sidebands, as a result of temperature gradients and ABMS effects, the line shape of the individual sidebands in a particular manifold that partially overlap in the one-dimensional spectrum is well resolved in the two-dimensional aMAT spectrum. A comparison of the aMAT spectrum with the conventional MAT spectrum (shown in Figure S7) clearly shows the advantage of using the SHAPs.

In order to access the isotropic spectrum, it proves convenient to project the two-dimensional spectrum onto the indirect dimension. The resulting spectra for all the  $\text{LiTMPO}_4$  compounds are shown in Figure 1c, with the conventional one-dimensional spectra in Figure 1b. The improvement in the spectral resolution evident by comparison of Figure 1b,c is striking, illustrating that the application of this experiment to other complex paramagnetic phases might readily provide access to interpretable spectra that would otherwise not be forthcoming from simpler techniques. The aMAT isotropic projections show a set of eight partially resolved peaks that are approximately equally spaced between the two bounding isotropic shifts corresponding to the pure  $\text{Mn}^{2+}$  and  $\text{Fe}^{2+}$  phases. The pure isotropic spectra display line shapes for individual sites that are wholly determined by the inhomogeneous contribution to the line width.

**3.2. Pathway Analysis of the  $\text{Fe}^{2+}$  and  $\text{Mn}^{2+}$  Contributions to the <sup>31</sup>P Fermi Contact Shifts.** The olivine structure of the  $\text{LiFe}_x\text{Mn}_{1-x}\text{PO}_4$  materials (Figure 1a) comprises a series of  $\text{PO}_4$  tetrahedra, and distorted  $\text{FeO}_6$  and

$\text{MnO}_6$  octahedra that are connected to form a set of one-dimensional channels occupied by the  $\text{Li}^+$  ions. Each <sup>31</sup>P contact shift is taken to arise as the sum over a set of individual hyperfine contributions corresponding to TM...P pathways comprising a single bridging O ion, i.e., TM–O–P, being labeled AB, C, D, E, and F in Figure 3a. Within this model, the total contact shift  $\delta^{\text{FC}}$  for a particular <sup>31</sup>P site may be written as

$$\delta^{\text{FC}} = \epsilon^{\text{AB}}(\text{M}^{\text{AB}}) + \epsilon^{\text{C}}(\text{M}^{\text{C}}) + \epsilon^{\text{D}}(\text{M}^{\text{D}}) + \epsilon^{\text{E}}(\text{M}^{\text{E}}) + \epsilon^{\text{F}}(\text{M}^{\text{F}}) \quad (1)$$

where  $\epsilon^{\text{P}}(\text{M}^{\text{P}})$  is the contribution from pathway P originating at a TM species  $\text{M}^{\text{P}}$ . Clearly, each of the five sites may be occupied by a cation drawn from either TM species, leading to a total of 32 distinct configurations (i.e., local environments) and a corresponding predicted maximum number of isotropic peaks for each spectrum.

The hybrid DFT calculations detailed earlier can assist here, providing not only the total contact shifts expected for the all-Mn and -Fe <sup>31</sup>P environments in LMP and LFP, respectively, but also the symmetry distinct pathway contributions and the differences between these values, defined as  $\Delta\epsilon^{\text{P}} = \epsilon^{\text{P}}(\text{Mn}^{2+}) - \epsilon^{\text{P}}(\text{Fe}^{2+})$ . While such a model is justifiable for the pure LMP and LFP phases, the use of these pathway contributions to interpret the NMR spectra of LFMP makes the implicit assumption that the mixing of  $\text{Mn}^{2+}$  and  $\text{Fe}^{2+}$  in the material does not lead to significant local distortions. To go beyond this hypothesis, we propose a simple model delimiting the effects of such distortions, this being to derive the contact shift pathway contributions for  $\text{Fe}^{2+}$  twice: once in the native LFP structure (denoted  $\text{Fe}@LFP$ ) and again in the fixed LMP structure ( $\text{Fe}@LMP$ ), and similarly for  $\text{Mn}^{2+}$  ( $\text{Mn}@LMP$  and  $\text{Mn}@LFP$ ). The pathway differences  $\Delta\epsilon^{\text{P}}$  defined above may now be separately derived in four ways, the resulting range of values providing insight into the sensitivity of each pathway to the effects of local structural distortions and establishing practical limits to such effects. Of course, it is likely that  $\text{Fe}^{2+}$  and  $\text{Mn}^{2+}$  each exert a conforming influence on their local coordination shells driving them to be similar to the same environments in the pure LFP and LMP phases, respectively, but it is clear that some degree of distortion away from these idealized geometries must occur in the mixed phases.

Table 1 presents the all-Fe and -Mn contact shifts, together with the differences in pathway contributions at hyb20 and hyb35. All of the pathway differences are positive, confirming that the half-filled 3d<sup>5</sup> configuration in  $\text{Mn}^{2+}$  leads to larger pathway contributions than the 3d<sup>6</sup> configuration in  $\text{Fe}^{2+}$ . This may be understood by reference to Figure 4, which shows the difference in spin density between LMP and LFP (both fixed in

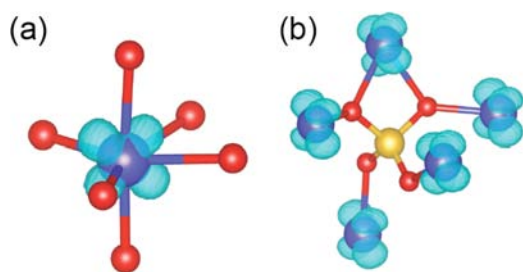


**Figure 4.** Isosurface of the spin density difference  $\rho^{\alpha-\beta}(\text{Mn@LFP}) - \rho^{\alpha-\beta}(\text{Fe@LFP})$  illustrating the d orbital that is singly occupied in  $\text{Mn}^{2+}$  and doubly occupied in  $\text{Fe}^{2+}$  shown relative to (a) the distorted  $\text{MO}_6$  octahedra and (b) TM–O–P bond pathways.

the LFP structure), effectively highlighting the TM 3d orbital that is singly occupied in  $\text{Mn}^{2+}$  and doubly occupied in  $\text{Fe}^{2+}$ . The significant distortions of the TM environments in LMP and LFP away from ideal octahedra mean that the orientation of this orbital relative to the coordinating O ions, as shown in Figure 4a, cannot be easily rationalized, but it is clear that the orbital adopts a nearly coplanar orientation relative to pathways C and D and a more orthogonal orientation relative to pathways AB, E, and F (Figure 4b). On this basis, we anticipate that the replacement of  $\text{Mn}^{2+}$  by  $\text{Fe}^{2+}$  should not only lead to a reduction in the shift contributions of all five pathways but also that the shift contributions of the former two pathways will be more strongly affected than those of the latter three, due to the greater suppression of the TM(d)–O(p $\pi$ )–P(s) spin delocalization mechanism in the geometry where the doubly occupied orbital in the  $3d^6$  configuration is coplanar with the bond pathway. The pathway differences presented in Table 1 confirm the predictions of this simple model.

The ranges presented in Table 1 also make clear that all of the pathway contributions are significantly affected by distortions, with the geometrically equivalent pathways E and F showing the greatest sensitivity. Further consideration of Figure 4 does not easily reveal why this should be so, emphasizing that such effects must be rather subtle. The pathway decompositions also confirm two more general but important points: First, that hyperfine couplings out to distances beyond the nearest TM–O–P shell may be safely neglected, their contributions amounting to not more than 59 ppm (or 0.6% of the total contact shift) in LMP and 26 ppm (0.8% of the total shift) in LFP. Second, they prove that the hyperfine couplings are additive over TM–P pairs to a high degree of accuracy, the differences between directly calculated shifts and the sums of the respective pathway contributions amounting to not more than 0.3% of the former across all geometries and functionals in LMP and to not more than 1.4% of the former in LFP.

As in the  $\text{Fe}^{3+}$  phosphates,<sup>20</sup> the hyb20 hyperfine parameters are all larger than the hyb35 values. The reasons for this trend with increasing HF exchange content are well-understood: the electronic self-interaction due to the classical Hartree term is incompletely canceled by the exchange–correlation functional at the pure DFT (hyb0) limit, leading to an excessive delocalization of spin density from TM to ligand sites. Meanwhile, pure HF and correlated HF (hyb100) theory are self-interaction free by construction and tend to underestimate the degree of spin delocalization. Our previous experience suggests that hybrid functionals in the intermediate range from

20 to 35% HF exchange provide hyperfine parameters in good agreement with experiment.<sup>20</sup>

The three aMAT spectra of the mixed  $x = 0.25, 0.5,$  and  $0.75$  samples were simultaneously fitted by varying the five pathway differences  $\Delta\epsilon^P = \epsilon^P(\text{Mn}^{2+}) - \epsilon^P(\text{Fe}^{2+})$  and the total contact shift of the all-Fe site, yielding six fit parameters in total. Initial values for the first five parameters were taken from the undistorted hyb20 DFT calculations (i.e., Mn@LMP, Fe@LFP). The fitting results are given in Table 1 and Figure 5, and

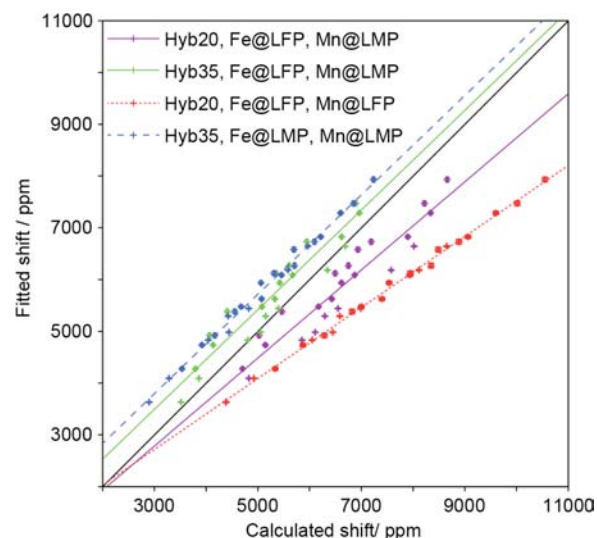


**Figure 5.** Comparison of the DFT calculated and fitted isotropic shifts for all 32 configurations shown in Figure 3a. The data plotted correspond to undistorted structures (hyb20 and hyb35, Fe@LFP and Mn@LMP) and the extremal trends induced by distortions for both functionals (hyb20 Fe@LFP and Mn@LFP, and hyb35 Fe@LFP and Mn@LMP). The best-fit linear correlations are shown for each of the four sets of calculated shifts. The solid black line shows the ideal trend. Error bars are shown for the fitted shifts.

the excellent quality of the fits is illustrated in Figure 3b. Examining Figure 5, it is clear that the fitted parameters are closest to the undistorted hyb35 values and that they depart significantly from the undistorted hyb20 values but in most cases remain within the bounds established by the limiting distortions model in combination with the hyb20 and hyb35 functionals. The notable exception to this is pathway C, where the fitted value lies somewhat below this range; the reasons for this remain unclear, but it does not amount to a substantial discrepancy. The full sets of calculated shifts for all the combinations are given in Figure S8 and Table S3.

Figure 5 plots the correlations between the DFT calculated and the fitted contact shifts of all 32 configurations shown in Figure 3a. Four data sets are shown, corresponding to the undistorted (Fe@LFP and Mn@LMP) hyb20 and hyb35 values with mean absolute errors (MAEs) relative to fitted values of 742 and 422 ppm, respectively, and the extremal distorted trends, namely (Fe@LFP and Mn@LFP) and (Fe@LMP and Mn@LMP) at hyb20 and hyb35, respectively, with significantly larger MAEs of 1687 and 714 ppm, respectively. These MAEs are significantly larger than the measured inhomogeneous line broadening in the aMAT projections of 140 ppm, and so it is clear that the experimental data are of sufficiently high resolution to discriminate between the various structural models used to account for the distortions. Furthermore, the data support the notion that the local environments of  $\text{Mn}^{2+}$

and  $\text{Fe}^{2+}$  in the LFMP phases are broadly rather similar to those occurring in the pure LMP and LFP phases, which is itself consistent with the finding that  $\text{Mn}^{2+}$  and  $\text{Fe}^{2+}$  apparently mix quite freely in LFMP.

Examining Figure 3b, it is clear that the basic assumptions of the present fitting model reproduce the experimental data well, providing support for the XRD findings of an essentially random distribution of  $\text{Mn}^{2+}$  and  $\text{Fe}^{2+}$  in LFMP across a broad range of stoichiometries.<sup>3–7</sup> The assignments of the spectra are given directly in Figure 3c. Efforts to use these findings to rationalize the spectra of partially electrochemically cycled phases are now underway.

#### 4. CONCLUSIONS

The work described above represents among the most complete set of analyses and interpretations of the NMR spectroscopic data of a class of paramagnetic materials obtained to date. The new aMAT NMR experiment incorporating state-of-the-art adiabatic pulse schemes is able to obtain broadband excitation and separation of the sideband patterns of complex paramagnetic materials at high magnetic field. Here, the application of this method to the study of lithium TM phosphate cathode materials shows how high-resolution site-specific information can be extracted for a range of isotropic shifts over a 1 MHz range with anisotropic shifts of hundreds of kHz. The set of shifts that was subsequently extracted has enabled a more thorough comparison with the results of DFT calculations than has generally been hitherto possible for such systems, including a rationalization of the shifts in terms of the different pathway contributions and a straightforward initial analysis of the effects of local distortions. Here we find that the distribution of Mn and Fe cations in LFMP is random across the  $x = 0.25, 0.5,$  and  $0.75$  stoichiometries and that Mn and Fe cosubstitution actually induces very little distortion in the mixed phases (where, for comparison, the differences between the P environments in the pure LMP and LFP phases amount to less than  $0.1 \text{ \AA}$  for TM–O–P bond distances and less than  $2^\circ$  for angles). Efforts to extend this combined approach to other mixed TM phases and to partially electrochemically cycled materials are now underway. It is our hope that such studies will provide a new and very detailed atomistic-level insight into the key processes occurring in these technologically important compounds.

#### ■ ASSOCIATED CONTENT

##### ■ Supporting Information

<sup>7</sup>Li NMR spectra of  $\text{LiFe}_x\text{Mn}_{1-x}\text{PO}_4$  ( $x = 0, 0.25, 0.5, 0.75, 1$ ), explanation of the refocusing properties of SHAPs in aMAT, details of the DFT calculations and experimental magnetic parameters, <sup>31</sup>P aMAT spectra of  $\text{LiFe}_x\text{Mn}_{1-x}\text{PO}_4$  ( $x = 0, 0.25, 0.5, 0.75, 1$ ), excitation bandwidths of square and SHAP RF pulses, comparison between <sup>31</sup>P MAT and aMAT spectra of  $\text{LiFe}_{0.25}\text{Mn}_{0.75}\text{PO}_4$ , details of the fitting, comparison of the fitted shifts with those calculated with hybrid 20%/35% DFT. This material is available free of charge via the Internet at <http://pubs.acs.org>.

#### ■ AUTHOR INFORMATION

##### Corresponding Author

[guido.pintacuda@ens-lyon.fr](mailto:guido.pintacuda@ens-lyon.fr)

##### Notes

The authors declare no competing financial interest.

#### ■ ACKNOWLEDGMENTS

We thank Benjamin Yunxu Zhu for helpful discussions and suggestions. We acknowledge financial support from the ANR programme blanc (ANR-08-BLAN-0035: PARA-NMR). An allocation of time upon the NANO computer cluster at the Centre for Functional Nanomaterials, Brookhaven National Laboratory, USA, which is supported by the U.S. Department of Energy, Office of Basic Energy Sciences, under contract no. DE-AC02-98CH10886 is also acknowledged. C.P.G.'s and D.S.M.'s membership of the U.K.'s HPC Materials Chemistry Consortium is gratefully acknowledged, as funded by the EPSRC (EP/F067496). This work made use of the facilities of HECToR, the U.K.'s national high-performance computing service, which is provided by UoE HPCx Ltd at the University of Edinburgh, Cray Inc. and NAG Ltd, and funded by the Office of Science and Technology through the EPSRC's High End Computing Programme. C.P.G. and M.S.W. thank NECCES (a DOE Energy Frontier Research Center, grant no. DE-SC0001294) for partial support (sample synthesis and DFT). Additional support for C.P.G., D.S.M. and F.C.S. comes from the EPSRC.

#### ■ REFERENCES

- (1) Padhi, A. K.; Nanjundaswamy, K. S.; Goodenough, J. B. *J. Electrochem. Soc.* **1997**, *144*, 1188.
- (2) Amine, K.; Yasuda, H.; Yamachi, M. *Electrochem. Solid-State* **2000**, *3*, 178.
- (3) Chen, Y. C.; Chen, J. M.; Hsu, C. H.; Yeh, J. W.; Shih, H. C.; Chang, Y. S.; Sheu, H. S. *J. Power Sources* **2009**, *189*, 790.
- (4) Hong, J.; Wang, F.; Wang, X.; Graetz, J. *J. Power Sources* **2011**, *196*, 3659.
- (5) Kim, J.; Park, K. Y.; Park, I.; Yoo, J. K.; Hong, J.; Kang, K. *J. Mater. Chem.* **2012**, *22*, 11964.
- (6) Yamada, A.; Chung, S. C. *J. Electrochem. Soc.* **2001**, *148*, A960.
- (7) Yao, J.; Bewlay, S.; Konstantinov, K.; Drozd, V. A.; Liu, R. S.; Wang, X. L.; Liu, H. K.; Wang, G. X. *J. Alloys Compd.* **2006**, *425*, 362.
- (8) Chen, Y. C.; Chen, J. M.; Hsu, C. H.; Lee, J. F.; Yeh, J. W.; Shih, H. C. *Solid State Ionics* **2009**, *180*, 1215.
- (9) Nedoseykina, T.; Kim, M. G.; Park, S. A.; Kim, H. S.; Kim, S. B.; Cho, J.; Lee, Y. *Electrochim. Acta* **2010**, *55*, 8876.
- (10) Wang, H.; Yang, Y.; Liang, Y.; Cui, L. F.; Casalongue, H. S.; Li, Y.; Hong, G.; Cui, Y.; Dai, H. *Angew. Chem., Int. Ed. Engl.* **2011**, *50*, 7364.
- (11) Saravanan, K.; Ramar, V.; Balaya, P.; Vittal, J. J. *J. Mater. Chem.* **2011**, *21*, 14925.
- (12) Grey, C. P.; Dupre, N. *Chem. Rev.* **2004**, *104*, 4493.
- (13) Baldus, M. *Angew. Chem., Int. Ed. Engl.* **2006**, *45*, 1186.
- (14) Blanc, F.; Coperet, C.; Lesage, A.; Emsley, L. *Chem. Soc. Rev.* **2008**, *37*, 518.
- (15) Bockmann, A. *Angew. Chem., Int. Ed. Engl.* **2008**, *47*, 6110.
- (16) Grey, C. P.; Tycko, R. *Phys. Today* **2009**, *62*, 44.
- (17) Tucker, M. C.; Doeff, M. M.; Richardson, T. J.; Finones, R.; Reimer, J. A.; Cairns, E. *J. Electrochem. Solid-State* **2002**, *5*, A95.
- (18) Wilcke, S. L.; Lee, Y. J.; Cairns, E. J.; Reimer, J. A. *Appl. Magn. Reson.* **2007**, *32*, 547.
- (19) Alla, M.; Lippmaa, E. *Chem. Phys. Lett.* **1982**, *87*, 30.
- (20) Kim, J.; Middlemiss, D. S.; Chernova, N. A.; Zhu, B. Y. X.; Masquelier, C.; Grey, C. P. *J. Am. Chem. Soc.* **2010**, *132*, 16825.
- (21) Ishii, Y.; Wickramasinghe, N. P.; Chimon, S. *J. Am. Chem. Soc.* **2003**, *125*, 3438.
- (22) Kervern, G.; Pintacuda, G.; Zhang, Y.; Oldfield, E.; Roukoss, C.; Kuntz, E.; Herdtweck, E.; Basset, J. M.; Cadars, S.; Lesage, A.; Coperet, C.; Emsley, L. *J. Am. Chem. Soc.* **2006**, *128*, 13545.
- (23) Wickramasinghe, N. P.; Shaibat, M.; Ishii, Y. *J. Am. Chem. Soc.* **2005**, *127*, 5796.

- (24) Kervern, G.; Pintacuda, G.; Emsley, L. *Chem. Phys. Lett.* **2007**, *435*, 157.
- (25) Nakashima, T. T.; Teymoori, R.; Wasylshen, R. E. *Magn. Reson. Chem.* **2009**, *47*, 465.
- (26) Nakashima, T. T.; Wasylshen, R. E.; Siegel, R.; Ooms, K. J. *Chem. Phys. Lett.* **2008**, *450*, 417.
- (27) Pell, A. J.; Kervern, G.; Emsley, L.; Deschamps, M.; Massiot, D.; Grandinetti, P. J.; Pintacuda, G. *J. Chem. Phys.* **2011**, *134*, 024117.
- (28) Siegel, R.; Nakashima, T. T.; Wasylshen, R. E. *J. Magn. Reson.* **2007**, *184*, 85.
- (29) Garwood, M.; DelaBarre, L. *J. Magn. Reson.* **2001**, *153*, 155.
- (30) Deschamps, M.; Kervern, G.; Massiot, D.; Pintacuda, G.; Emsley, L.; Grandinetti, P. J. *J. Chem. Phys.* **2008**, *129*, 204110.
- (31) Antzutkin, O. N.; Shekar, S. C.; Levitt, M. H. *J. Magn. Reson., Ser. A* **1995**, *115*, 7.
- (32) Dixon, W. T. *J. Magn. Reson.* **1981**, *44*, 220.
- (33) Dixon, W. T. *J. Chem. Phys.* **1982**, *77*, 1800.
- (34) Gann, S. L.; Baltisberger, J. H.; Pines, A. *Chem. Phys. Lett.* **1993**, *210*, 405.
- (35) Hu, J. Z.; Alderman, D. W.; Ye, C. H.; Pugmire, R. J.; Grant, D. M. *J. Magn. Reson., Ser. A* **1993**, *105*, 82.
- (36) Hung, I.; Zhou, L.; Pourpoint, F.; Grey, C. P.; Gan, Z. *J. Am. Chem. Soc.* **2012**, *134*, 1898.
- (37) Chen, J. J.; Vacchio, M. J.; Wang, S. J.; Chernova, N.; Zavalij, P. Y.; Whittingham, M. S. *Solid State Ionics* **2008**, *178*, 1676.
- (38) Yang, S. F.; Zavalij, P. Y.; Whittingham, M. S. *Electrochem. Commun.* **2001**, *3*, 505.
- (39) Hwang, T. L.; van Zijl, P. C.; Garwood, M. *J. Magn. Reson.* **1998**, *133*, 200.
- (40) Bachmann, P.; Aue, W. P.; Muller, L.; Ernst, R. R. *J. Magn. Reson.* **1977**, *28*, 29.
- (41) Keeler, J.; Neuhaus, D. *J. Magn. Reson.* **1985**, *63*, 454.
- (42) (a) Dovesi, R.; Saunders, V. R.; Roetti, C.; Orlando, R.; Zicovich-Wilson, C. M.; Pascale, F.; Civarelli, B.; Doll, K.; Harrison, N. M.; Bush, I. J.; D'Arco, P.; Llunell, M. *CRYSTAL09 User's Manual*; University of Torino: Torino, Italy, 2009. (b) Dovesi, R.; Orlando, R.; Civalieri, B.; Roetti, C.; Saunders, V. R.; Zicovich-Wilson, C. M. *Z. Kristallogr.* **2005**, *220*, 571–573, DOI: 10.1524/zkri.220.5.571.65065.
- (43) Muscat, J.; Wander, A.; Harrison, N. M. *Chem. Phys. Lett.* **2001**, *342*, 397.
- (44) Cora, F.; Alfredsson, M.; Mallia, G.; Middlemiss, D. S.; Mackrodt, W. C.; Dovesi, R.; Orlando, R. *Struct. Bonding (Berlin)* **2004**, *113*, 171.
- (45) Feng, X. B.; Harrison, N. M. *Phys. Rev. B* **2004**, *70*, 092402.
- (46) Middlemiss, D. S.; Lawton, L. M.; Wilson, C. C. *J. Phys.: Condens. Matter* **2008**, *20*.
- (47) Moreira, I. D. R.; Illas, F.; Martin, R. L. *Phys. Rev. B* **2002**, *65*, 155102.
- (48) Chernova, N. A.; Nolis, G. M.; Omenya, F. O.; Zhou, H.; Li, Z.; Whittingham, M. S. *J. Mater. Chem.* **2011**, *21*, 9865.
- (49) Tucker, M. C.; Doeff, M. M.; Richardson, T. J.; Finones, R.; Cairns, E. J.; Reimer, J. A. *J. Am. Chem. Soc.* **2002**, *124*, 3832.
- (50) Conolly, S.; Glover, G.; Nishimura, D.; Macovski, A. *Magn. Reson. Med.* **1991**, *18*, 28.